Mathematical modeling of erosion and deposition in porous media

Hamad El Kahza [1,*] and Pejman Sanaei [2,†]

[1]*Department of Mathematical Sciences, University of Delaware, Newark, Delaware 19716, USA*
[2]*Department of Mathematics and Statistics, Georgia State University, Atlanta, Georgia 30302, USA*

Erosion and deposition are represented as the evolution of solid bodies due to the forces exerted by the fluid or air on the contact surfaces, which both often lead to reconfiguration and change of the topology and structure of the porous media. These processes are notably very complicated and challenging to study. In this work, we formulate simplified and idealized mathematical models to examine the internal evolution of flow networks in the setting of cylindrical channels, undergoing a unidirectional flow, by using asymptotic and numerical techniques. Starting from the Stokes equations combined with the advection-diffusion equation for solid transport, we propose a model to construct a complete analysis of both the erosion and deposition. The considered approach is of the form of threshold laws: the fluid-solid interface erosion and deposition occur when the total shear stress is, respectively, greater or lower than some specified critical values, depending on the solid material. As a consequence of the erosion and deposition, the radii of the channels in the structure expand and shrink, respectively, due to several key parameters, which we find and investigate in this paper. We also perform a parametric study to quantify the correlation between these threshold values and the particle concentration in the flow. A comprehensive parametric study of the constructed model reveals that the final configuration of the structure can be predicted from the system parameters.

I. INTRODUCTION

Erosion and deposition of particles alter the solid interface and the internal morphology of porous media, which as a consequence affect the flow property: notably the fluid velocity, the exerted shear stress by the flow, and the particle concentration in the feed. These two processes are ubiquitous in nature as well as industry; therefore investigating them is instrumental to address their desirability within fluid flow systems. Specific easily observable examples from geomorphology include soil erosion and land degradation (due to wind or floodwaters), erosion of riverbanks [1,2], and formation of yardangs or pillar and toadstool-shaped rock formations known as hoodoos (due to wind erosion) [3,4]. Less obvious examples found in biology include the formation of arterial plaques, bacterial colonies known as biofilms, as well as the erosion and particle deposition in porous media and membrane filters [5–9].

In the environmental context, erosion represents the destruction of mass as a result of forces exerted on the contact interface between a solid and fluid phase over a long period. For instance, tunnel erosion is one type of erosion caused by water penetrating through a hole in a subsurface; parts of the soil are carried away with flow, which leaves behind a small tunnel underneath the surface. The tunnel becomes larger due to water flow resulting in a substantial likelihood for the

---
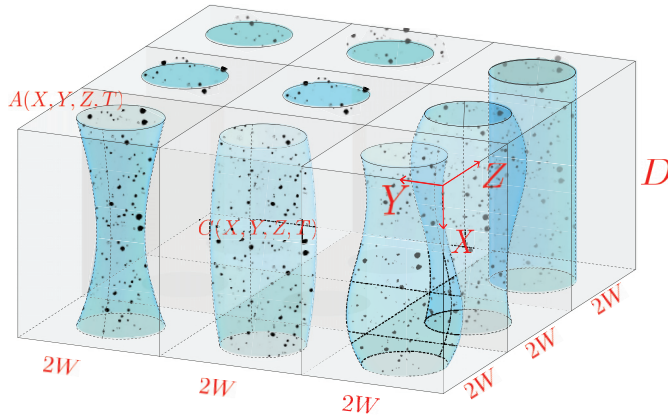
*helkahza@udel.edu
†psanaei@gsu.edu

FIG. 1. Schematic showing a structure and channels with the channel radii $A(X, Y, Z, T)$ and particle concentration $C(X, Y, Z, T)$.

soil to collapse. Generally speaking, in geological contexts, erosion of solid bodies and deposition of debris on or into them are essential in carving and shaping various morphologies in nature and the environment. The interactions of air and water with the earth's surface have been modeled and studied by many researchers (see, for example, [10–12] and references therein). Similarly, fluid flow can erode the internal structure of a porous medium and/or deposit particles there. This leads to an evolution in the morphology of the porous medium, which results in a change in the flow path [13–18].

Depending on the flow and the porous medium structure, two scenarios are of interest to consider in modeling of the erosion and deposition processes: (1) external and (2) internal flow within the porous media. In the former case, it is assumed that the structure has a gradient in porosity and consists of a collection of solid obstacles or fibers, which fluid flows around [19,20]. On the other hand, for the internal flow, which is the focus of this paper, the structure is assumed to consist of slender channels/pores that span the structure from upstream to downstream side, and the viscous fluid flow moves inside the channels/pores [21,22], as shown in Fig. 1. One may consider internal erosion in structures such as embankment dams [23] and porous media, which can be interpreted as reverse deposition and filtration processes. There are, therefore, many mathematical similarities in the modeling of erosion and deposition processes. The purpose of our modeling effort is to propose a model tracing the erosion/deposition occurrence and their influences on a porous medium structure, given specific identifiable parameters.

Numerous numerical schemes have been developed by researchers to model the erosion process [24]. One of the approaches is the resolved computational fluid dynamics (CFD) method. Considerable effort has been devoted to analyze and conduct this direct method. The fluid flow and particle interactions are investigated through basic empirical systems of formulas, where the governing equations are being solved using finite element method (FEM); i.e., the Navier-Stokes equations are simulated using a collocated mesh grid in which the channel geometry defines the structure [25,26]. Each step taken towards convergence is expensive, and adaptive remeshing is often used to account for microstructure evolution. Therefore, many other authors considered a second approach using an unresolved CFD approach consisting of a coupled hybrid model. Various works adopted this newly emerged technique to investigate further the fluid path after a reconfiguration of the system structure [27,28]. This technique is less expensive to implement and solves the considered equations on fluid cells much larger than the channel-scale level. It does not require remeshing, and thus, the microscopic description of the problem is comparatively inefficient.

Another approach is the lattice Boltzmann method (LBM), which relies on discretizing the particle-based model. In LBM, the flow is solved for on a channel-scale level, replacing the Navier-Stokes equations by the discrete Boltzmann equation. The fluid/particle behavior is resolved through interpolation and extrapolation schemes, modeling the Navier-Stokes equations beyond the known points by drawing a likely approximate form through a fixed lattice [13,14,29]. Similar to CFD, this technique simulate the fluid behavior by discretizing the flow velocity vectors relative to the channel scale. Despite its ability to resolve a three-dimensional lattice, the LBM is an expensive method to implement and requires high computation power. The fourth approach is the pore network model (PNM), which consists of simplifying the system geometry into channel spaces interconnected via their respective inlet structure. In this method the complexity of the flow is reduced to the exchange laws between the adjacent edges. The formulation of the flow equation is based on the assumption of a unique pressure at each computational node. This technique achieves high-resolution accuracy with lower computing costs for small-scale domains, compared with other simulation methods such as LBM [24,30].

In this paper, we take an integrated approach to formulate and study mathematical models of erosion and deposition in reconfigurable flow networks, specifically in porous media, alongside analytically exact validation from experimental data in the literature [16,17,31]. The experiments will help calibrate and validate our mathematical models and of course are much cheaper than gathering data from real-world examples. Modeling erosion and deposition are still computationally complex, and the choice of the computational approach implicates limitations on uncovering channel-scale behaviors. Numerical implementations are limited to a small-scale analysis of the erosive behavior in the setting of a channel or other geometries undergoing the Stokes flow. Implementing an erosion-deposition model still poses complex numerical challenges and therefore has been confined to date to the LBM method. This uses parallel computing, which again poses limitations on unveiling the coarse-grained description behind these phenomena. Our work aims to cover this gap in the literature by capturing the different regimes in the fluid-structure interaction in a channel subject to erosion and deposition. The derivation of analytical solutions allows classifying behavior of expansion or clogging in porous media according to the dimensionless parameters in the governing equations.

This paper is organized as follows: in Sec. II, we introduce the mathematical models for the flow in a porous medium channel, as well as the governing equations for the particle concentration in the feed. In Sec. III, we introduce appropriate scalings, for the flow and particle concentration, to nondimensionalize the models from Sec. II. Then, in Sec. IV, we present the simulations of channel evolution due to the erosion and deposition of particles. We also compare and validate our models and results with the experimental literature. Finally, we summarize our modeling results in Sec. V and provide some insight into real-world applications as well.

II. MODEL FORMULATION

We assume that the porous medium consists of an array of axisymmetric channels, with thickness D. It lies in the (Y, Z) plane in a flat way and the unidirectional viscous flow passes the structure in the positive X direction as the basic setup is schematized in Fig. 1. The structure morphology and flow does not necessarily need to be assumed homogeneous in the (Y, Z) plane; therefore the solution for the flow within each channel of radius $A(X, Y, Z, T)$, enclosed in a box of $2W \times 2W \times D$, can be obtained in the cylindrical coordinates (R, θ, X) in which properties vary only in the special directions X, the radial direction R, and time T. While considering channels of different sizes and shapes would offer a more comprehensive understanding of erosion and deposition processes, our primary objective in this work is to analyze a single representative channel. Extending our model to accommodate nonidentical channels would require a thorough analysis based on homogenization theory [32–34], which is beyond the scope of this study. Therefore, without loss of generality, one can consider only one channel or pore, drop Y and Z dependency and formulate the model, and replicate the results in the (Y, Z) plane for the rest of the channels. Therefore, for brevity, we

consider the channel radius is $A(X, T)$ with small aspect ratio $\epsilon = W/D \ll 1$, while for the internal structure, it is assumed to be axisymmetric and identical [35–37]; however, it may change in the X and R directions. Our model represents the average state across the (Y, Z) cross section of the structure, where spatial fluctuations in the plane of the structure are present. Needless to say, in reality, the structure has a much more sophisticated topology, and most structures have a rather complex morphology [20,38–41]. Note that we consider an incompressible Newtonian fluid and the transport of eroded and dilute suspension of particles via advection and diffusion through the structure, which evolves in the course of time.

A. Stokes equations

Note that stars on the dependent variables here indicate R dependence, while the unstarred dependent variables are averaged over the channel/pore cross section. There are two timescales introduced in our model: the first one comes from the flow velocity and the second one is originated from the rate of change in the channel radius due to particle erosion/deposition. Since the timescale associated with the evolution of the porous medium morphology due to particle erosion/deposition is much longer compared to the one originated from the flow velocity, we employ a quasistatic model, where we consider the domain of the flow as $0 \leqslant R \leqslant A$ and $0 \leqslant X \leqslant D$. The channel velocity vector $\boldsymbol{U}_p^*(R, X, T)$ is defined as $\boldsymbol{U}_p^* = (V_p^*, 0, U_p^*)$ and the pressure $P^*(R, X, T)$ satisfies the Stokes equations (the Reynolds number is small in many erosion/deposition scenarios [13,16,18,31,42]). Therefore, we have

$$\boldsymbol{\nabla} P^* = \mu \nabla^2 \boldsymbol{U}_p^*, \quad \boldsymbol{\nabla} \cdot \boldsymbol{U}_p^* = 0, \quad 0 \leqslant X \leqslant D, \quad 0 \leqslant R \leqslant A, \tag{1}$$

where μ is the fluid viscosity. The Stokes equation is subject to the continuity of the mass flux of eroded and deposited material [43] and no-slip boundary conditions

$$\dot{M} = \rho(V_n - \boldsymbol{U}_p^* \cdot \boldsymbol{n}), \quad \boldsymbol{U}_p^* \cdot \boldsymbol{t} = 0 \quad \text{at} \quad R = A, \tag{2}$$

where $\dot{M}$ is the total flux of eroded or deposited material per unit area, ρ is the total density of the fluid and particles per unit area, V_n is the normal velocity of the channel wall, and $\boldsymbol{n}$ and $\boldsymbol{t}$ are the unit normal and tangent vectors to the channel wall, respectively, where

$$\boldsymbol{n} \parallel \boldsymbol{\nabla}(R - A). \tag{3}$$

We consider a constant pressure-driven flow scenario here, therefore the boundary conditions for the pressure $P^*(X, T)$ across the structure are

$$P^*|_{X=0} = P_{\text{in}}, \quad P^*|_{X=D} = 0. \tag{4}$$

In addition, the total shear stress $\Sigma(R, X, T)$ at the channel walls, exerted by the flow [41,44], is given by

$$\Sigma = \mu\big(\boldsymbol{\nabla} \boldsymbol{U}_p^* + \boldsymbol{\nabla} \boldsymbol{U}_p^{*\mathsf{T}}\big)\boldsymbol{n} \cdot \boldsymbol{t}|_{R=A}, \tag{5}$$

where the superscript T denotes the transpose of the matrix. The modeling challenge here is how to link the fluid channel velocity $\boldsymbol{U}_p^*$ to measurable particle concentration characteristics in order to obtain a predictive model of erosion deposition coincides with experiments and reality.

B. Advection-diffusion equation

The channel radius varies in the porous-medium depth, and the system dynamics are tracked over time as the internal morphology of the porous medium changes due to the particle erosion and deposition. This can be modeled by a particle concentration C^* that varies with channel depth X, radius R, and time T. In general, particles are advected and diffuse within the flow, and are eroded from or adhered to the channel wall, at rates determined by a detailed and careful asymptotic analysis of the governing advection-diffusion model. The channel radius $A(X, T)$ expands and

shrinks in response to the erosion and deposition, respectively. While considering particles relative inertia and particle-particle interactions would offer a more comprehensive understanding of erosion and deposition processes, our primary objective in this work is to analyze particle erosion and deposition, in the dilute suspension limit, through the porous medium. Extending our model to accommodate particles' relative inertia and particle-particle interactions would require a thorough analysis based on the boundary integral method, which is beyond the scope of this study. The full advection-diffusion equation for the particles with concentration $C^*(R, X, T)$ follows

$$\frac{\partial C^*}{\partial T} + \nabla \cdot \boldsymbol{Q}_c^* = 0, \quad \boldsymbol{Q}_c^* = -\Xi \nabla C^* + \boldsymbol{U}_p^* C^*, \tag{6}$$

where $\boldsymbol{Q}_c^*(R, X, T)$ is the flux of total particles, and Ξ is the diffusion coefficient of particles, with the boundary conditions [7,13,45]

$$C^*|_{X=0} = C_{\text{in}}, \quad \left.\frac{\partial C^*}{\partial X}\right|_{X=D} = 0, \quad \boldsymbol{Q}_c^* \cdot \boldsymbol{n} = \left.\frac{\Lambda_e}{2}\Sigma H\right|_{\Sigma - \Sigma_e} - \left.\frac{\Lambda_d}{2}C^* H\right|_{\Sigma_d - \Sigma} \quad \text{at} \quad R = A, \tag{7}$$

where H is the Heaviside function defined as

$$H(\Sigma) = \begin{cases} 0 & \text{if} \quad \Sigma < 0, \\ 1 & \text{if} \quad \Sigma \geqslant 0. \end{cases} \tag{8}$$

Here Σ_e and Σ_d are the erosion and deposition shear stress thresholds depending on the eroded material, C_{in} is the particle concentration at the channel inlet, and Λ_e and Λ_d are the erosion and the stickiness coefficients, respectively. The second boundary condition in (7) enforces that the particle concentration does not change at the channel outlet [45]. The last boundary condition is a general particle erosion and deposition law at the channel wall, describing erosion and deposition, when the total shear stress is, respectively, greater and lower than some specific threshold values. Since the model is assumed to be quasistatic, we have the steady-state form of the advection-diffusion equation as

$$\Xi \left[\frac{1}{R}\frac{\partial}{\partial R}\left(R\frac{\partial C^*}{\partial R}\right) + \frac{\partial^2 C^*}{\partial X^2}\right] = V_p^* \frac{\partial C^*}{\partial R} + U_p^* \frac{\partial C^*}{\partial X}. \tag{9}$$

Note that to obtain (9) from (6), we use the continuity equation, $\nabla \cdot \boldsymbol{U}_p^* = 0$, given in (1). Moreover, with the assumption that $\boldsymbol{n} \| \nabla(R - A(X))$, the wall deposition boundary condition given in (7), becomes

$$\Xi \frac{\partial C^*}{\partial R} - \Xi \frac{\partial C^*}{\partial X}\frac{\partial A}{\partial X} = \left.\frac{\Lambda_e}{2}\Sigma H\right|_{\Sigma - \Sigma_e} - \left.\frac{\Lambda_d}{2}C^* H\right|_{\Sigma_d - \Sigma}, \quad \text{at} \quad R = A. \tag{10}$$

To gain further insight into the dynamics of flow through the channel, we define the averaged version of the channel velocity $\boldsymbol{U}_p = (V_p, 0, U_p)$, the pressure P, and the particle concentration C as

$$y = \frac{1}{\pi A^2}\int_0^A \int_0^{2\pi} y^* R \, \mathrm{d}\theta \, \mathrm{d}R, \quad y \in \{V_p, U_p, P, C\}. \tag{11}$$

C. Erosion and deposition models

Erosion stems from the removal of solid particles by the fluid-mechanical shear stress, when it is more than some specific threshold Σ_e, whereas below a lower threshold Σ_d the adhesive force of the suspended particles is dominant and deposition occurs [11,13,16,18,31,42,44,46]. Note that no erosion and deposition happen when the total shear stress exerted by the fluid flow lies between these two thresholds, Σ_e and Σ_d. Therefore, the suggested model for erosion and deposition follows

$$\frac{\dot{M}}{\rho_s} = \underbrace{B_e\left(\Sigma - \Sigma_e\right) H|_{\Sigma - \Sigma_e}}_{\text{erosion}} - \underbrace{B_d\, C\left(\Sigma_d - \Sigma\right) H|_{\Sigma_d - \Sigma}}_{\text{deposition}}, \quad \text{at} \quad R = A, \tag{12}$$

where ρ_s is the density of the solid wall. B_e and B_d are the erosion and deposition coefficients, respectively, depending on the properties of the solid structure such as the cohesive forces [11,13,16,18,31,42,44,46]. Note that B_e and B_d depend on the erosion and the stickiness coefficients, Λ_e and Λ_d, respectively. We consider $B_e = \alpha_e \Lambda_e$ and $B_d = \alpha_d \Lambda_d$, where $\alpha_e = \alpha_d$ is related to the particle size [22]. Note that the channel wall normal velocity is related to the channel radius by

$$V_n = \frac{\partial A}{\partial T}\left[1 + \left(\frac{\partial A}{\partial X}\right)^2\right]^{-1/2}, \tag{13}$$

and the initial channel radius is prescribed

$$A|_{T=0} = A_{\text{in}}, \tag{14}$$

where $A_{\text{in}}(X)$.

III. SCALING AND NONDIMENSIONALIZATION

In this section, we use the following scalings to nondimensionalize the presented models (1)–(14) in order to reduce the number of independent parameters:

$$(U_p^*, V_n) = \frac{W^2 P_{\text{in}}}{\mu D}(u_p^*, v_n), \quad X = Dx, \quad (A, R) = W(a, r), \quad P^* = P_{\text{in}} p^*, \quad C^* = C_{\text{typ}} c^*,$$

$$(\Sigma, \Sigma_d, \Sigma_e) = \frac{W P_{\text{in}}}{2D}(\tau, \tau_d, \tau_e), \quad T = \frac{\mu D}{W P_{\text{in}}}t, \quad H(\Sigma) = h(\tau), \quad \dot{M} = \frac{\rho W^2 P_{\text{in}}}{\mu D}\dot{m}, \tag{15}$$

where $u_p^*(r, x, t)$ defined as $u_p^* = (\epsilon v_p^*, 0, u_p^*)$ is the dimensionless channel velocity and C_{typ} is a typical value for the particle concentration.

A. Stokes equations

With the scalings in (15), the Stokes equations (1) become

$$\frac{1}{\epsilon^2}\frac{\partial p^*}{\partial r} = \frac{1}{r}\frac{\partial}{\partial r}\left(r\frac{\partial v_p^*}{\partial r}\right) + \epsilon^2\frac{\partial^2 v_p^*}{\partial x^2} - \frac{v_p^*}{r^2}, \tag{16}$$

$$\frac{\partial p^*}{\partial x} = \frac{1}{r}\frac{\partial}{\partial r}\left(r\frac{\partial u_p^*}{\partial r}\right) + \epsilon^2\frac{\partial^2 u_p^*}{\partial x^2}, \tag{17}$$

$$\frac{1}{r}\frac{\partial(r v_p^*)}{\partial r} + \frac{\partial u_p^*}{\partial x} = 0. \tag{18}$$

The dimensional boundary condition (2) can be simplified as

$$\dot{m} = v_n - \epsilon\left(v_p^* - u_p^*\frac{\partial a}{\partial x}\right), \quad u_p^* + \epsilon^2 v_p^*\frac{\partial a}{\partial x} = 0, \quad \text{at} \quad r = a, \tag{19}$$

since

$$\boldsymbol{n} = \frac{1}{\sqrt{1 + \left(\epsilon\frac{\partial a}{\partial x}\right)^2}}\left(1, 0, -\epsilon\frac{\partial a}{\partial x}\right), \quad \boldsymbol{t} = \frac{1}{\sqrt{1 + \left(\epsilon\frac{\partial a}{\partial x}\right)^2}}\left(\epsilon\frac{\partial a}{\partial x}, 0, 1\right), \tag{20}$$

obtained from (3) and (15). The dimensionless pressure boundary conditions in (4), after scaling, become

$$p^*|_{x=0} = 1, \quad p^*|_{x=1} = 0. \tag{21}$$

We now introduce expansion of all dependent variables in powers of ϵ:

$$y(x, r, t) = y_0(x, r, t) + \epsilon y_1(x, r, t) + \epsilon^2 y_2(x, r, t) + \cdots, \quad y, y_i \in \{p, p^*, v_p, v_p^*, u_p, u_p^*, c, c^*, \tau\},$$

$$\times \, i \in \{0, 1, 2, \dots\}. \tag{22}$$

From (16) and (22), we obtain that the pressure p^* is independent of the radial coordinate r at the leading order, $p_0^*(t) = p_0^*(x, t)$. Solving for the leading order channel velocity (17) and (18) along with the boundary conditions (19) and (21) yields the leading orders channel velocity and pressure, respectively,

$$u_{p_0}^* = \frac{1}{4} \frac{dp_0^*}{dx}(r^2 - a^2), \quad v_{p_0}^* = -\frac{1}{16} \frac{\partial}{\partial x}\left(\frac{dp_0^*}{dx}(r^3 - 2a^2 r)\right), \quad p_0^* = \frac{\int_x^1 \frac{dx'}{a^4(x', t)}}{\int_0^1 \frac{dx'}{a^4(x', t)}}. \tag{23}$$

So far, we have solved the Stokes equations in a single porous medium channel. Using the same velocity scalings for (11) as in (15), the dimensionless cross-sectionally averaged [see (11)] channel fluid velocity $\boldsymbol{u}_p(x, t)$, which is defined as $\boldsymbol{u}_p = (\epsilon v_p, 0, u_p)$, and the pressure $p(x, t)$ become, to leading order,

$$u_{p_0} = -\frac{1}{8} a^2 \frac{\partial p_0}{\partial x}, \quad v_{p_0} = \frac{1}{8a^2}\left(\frac{7}{15} \frac{\partial^2 p_0}{\partial x^2} a^5 + \frac{4}{3} \frac{\partial p_0}{\partial x} \frac{\partial a}{\partial x} a^4\right), \quad p_0 = \frac{\int_x^1 \frac{dx'}{a^4(x', t)}}{\int_0^1 \frac{dx'}{a^4(x', t)}}. \tag{24}$$

We now continue to find a simplified solution to the shear stress. Using (15), (20), and (22) together in the total shear stress equation (5), after some manipulations, gives the dimensionless shear stress at leading order $\tau_0(x, t)$

$$\tau_0 = 2 \left.\frac{\partial u_{p_0}^*}{\partial r}\right|_{r=a}. \tag{25}$$

We further simplify (25) by using the expressions for the axial channel velocity and pressure, $u_{p_0}^*$ and p_0^*, respectively, given in (23) to obtain

$$\tau_0 = \frac{1}{a^3(x, t) \int_0^1 \frac{dx}{a^4(x, t)}}. \tag{26}$$

B. Advection-diffusion equation

We can find a simplified solution to the advection-diffusion equation and nondimensionalize (7), (9), and (10) using the scalings in (15), to arrive at

$$\frac{1}{\epsilon^2 \text{Pe}}\left[\frac{1}{r} \frac{\partial}{\partial r}\left(r \frac{\partial c^*}{\partial r}\right) + \epsilon^2 \frac{\partial^2 c^*}{\partial x^2}\right] = v_p^* \frac{\partial c^*}{\partial r} + u_p^* \frac{\partial c^*}{\partial x}, \qquad \text{Pe} = \frac{W^2 P_{\text{in}}}{\mu \Xi}, \tag{27}$$

with the dimensionless boundary conditions

$$c^*|_{x=0} = c_{\text{in}}, \quad \left.\frac{\partial c^*}{\partial x}\right|_{x=1} = 0, \quad \frac{1}{\epsilon^2 \text{Pe}} \frac{\partial c^*}{\partial r} - \frac{1}{\text{Pe}} \frac{\partial c^*}{\partial x} \left.\frac{\partial a}{\partial x}\right|_{r=a} = \left.\frac{\lambda_e}{2} \tau h\right|_{\tau - \tau_e} - \left.\frac{\lambda_d}{2} c^* h\right|_{\tau_d - \tau},$$

$$\text{at} \quad r = a, \quad \lambda_e = \frac{\Lambda_e \mu D}{2W^2 C_{\text{typ}}}, \quad \lambda_d = \frac{\Lambda_d \mu D^2}{W^3 P_{\text{in}}}, \tag{28}$$

where Pe is the particles Péclet number, describing the ratio of advective to diffusive transport rates of particles. λ_e and λ_d are the dimensionless erosion and stickiness coefficients, respectively. By using (22) and conducting asymptotic analysis for (27), we find that the particle concentration and therefore their cross-sectionally averaged forms, at $O(1)$ and $O(\epsilon)$ are independent of r, as a result,

$$c_0^* = c_0, \quad c_1^* = c_1. \tag{29}$$

At $O(1)$, (27) reduces to

$$\frac{1}{\text{Pe}}\left[\frac{1}{r}\frac{\partial}{\partial r}\left(r\frac{\partial c_2^*}{\partial r}\right) + \frac{\partial^2 c_0^*}{\partial x^2}\right] = u_{p_0}^*\frac{\partial c_0^*}{\partial x}. \tag{30}$$

Applying the dimensionless version of the cross-sectionally averaged operator given in (11) on (30) gives

$$-\frac{2}{a}\frac{1}{\text{Pe}}\left.\frac{\partial c_2^*}{\partial r}\right|_{r=a} = \frac{1}{\text{Pe}}\frac{\partial^2 c_0}{\partial x^2} - u_{p_0}\frac{\partial c_0}{\partial x}. \tag{31}$$

Note that the third boundary condition in (28) reduces to $\frac{\partial c_0^*}{\partial r}|_{r=a} = 0$ and $\frac{\partial c_1^*}{\partial r}|_{r=a} = 0$, respectively, which are consistent with (29). In addition, the third boundary condition in (28) at $O(1)$, along with (29) and (31) yields

$$\frac{1}{\text{Pe}}\frac{\partial c_2^*}{\partial r} - \frac{1}{\text{Pe}}\frac{\partial c_0}{\partial x}\frac{\partial a}{\partial x} = \left.\frac{\lambda_e}{2}\tau_0 h\right|_{\tau_0-\tau_e} - \left.\frac{\lambda_d}{2}c_0 h\right|_{\tau_d-\tau_0}, \quad \text{at} \quad r = a. \tag{32}$$

Combining (31) and (32), we obtain the full dimensionless advection-diffusion equation as

$$-\frac{1}{\text{Pe}}\frac{\partial^2 c_0}{\partial x^2} + \left(u_{p_0} - \frac{2}{a\text{Pe}}\frac{\partial a}{\partial x}\right)\frac{\partial c_0}{\partial x} - \left.\frac{\lambda_e}{a}\tau_0 h\right|_{\tau_0-\tau_e} + \left.\frac{\lambda_d}{a}c_0 h\right|_{\tau_d-\tau_0} = 0, \tag{33}$$

where

$$\lambda_e = \frac{\Lambda_e\mu D}{2W^2 C_{\text{typ}}}, \quad \lambda_d = \frac{\Lambda_d\mu D^2}{W^3 P_{\text{in}}}, \quad h(\tau) = \begin{cases} 0 & \text{if} \quad \tau < 0, \\ 1 & \text{if} \quad \tau \geqslant 0, \end{cases} \tag{34}$$

subject to the boundary conditions

$$c_0|_{x=0} = c_{\text{in}}, \quad \left.\frac{\partial c_0}{\partial x}\right|_{x=1} = 0, \tag{35}$$

obtained from (28).

C. Erosion and deposition models

By using the scalings (15) in the dimensional erosion model (12) along with (13), (19), and (20) at the leading order, we find the dimensionless erosion model as

$$\frac{\partial a}{\partial t} = \underbrace{\beta_e(\tau_0 - \tau_e)h|_{\tau_0-\tau_e}}_{\text{erosion}} - \underbrace{\beta_d c_0(\tau_d - \tau_0)h|_{\tau_d-\tau_0}}_{\text{deposition}}, \quad \beta_e = \frac{\rho_s B_e\mu}{2\rho W}, \quad \beta_d = \frac{\rho_s B_d\mu C_{\text{typ}}}{2\rho W}, \tag{36}$$

with the prescribed initial channel radius

$$a|_{t=0} = a_{\text{in}}, \tag{37}$$

which is obtained from (14). An interaction between the liquid phase and the channel solid wall occurs due to the particle erosion and deposition. After dropping subscripts 0 from the leading-order parameters u_{p_0}, τ_0, c_0, τ_{e_0}, and τ_{d_0} in (24), (26), (33), (35), and (36), we present the schematic diagram in Fig. 2 describing the flow and channel interactions as below:

(1) For a given initial channel profile, the flow velocity and shear stress are calculated by (24) and (26), respectively.

(2) With those, the particle transport equation [see (33)] gives the particle concentration along the channel axis.

(3) The channel radius will be updated due to erosion and deposition according to (36) based on the shear stress and the particle concentration calculated in steps 1 and 2.
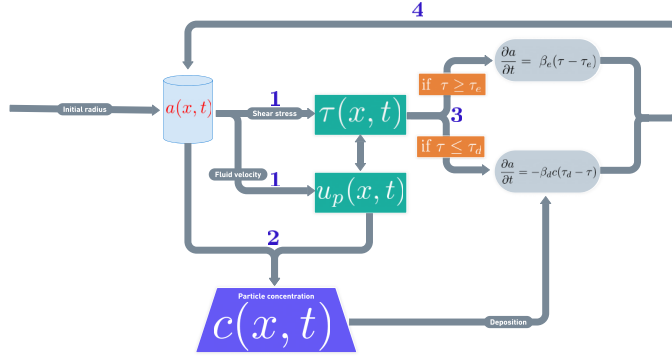
(4) Return to step 1.

FIG. 2. Erosion and deposition system diagram.

IV. RESULTS

In this section, we use several dimensionless key parameters summarized in Table II, which are based on the dimensional parameters given in Table I. These parameters affect the occurrence of erosion and deposition in the porous-medium channels. Our model is based on several key dimensionless parameters for erosion and deposition as well as functional inputs. The Péclet number Pe describes the ratio of advective to diffusive transport rates of particles. As the Péclet number tends to infinity, the diffusive transport vanishes, resulting in an advection-only model. On the other hand, the transport model becomes more diffusive as Péclet number approaches zero. The erosion coefficient, λ_e, characterizes the erodibility of the solid interface and is a material-dependent parameter. The stickiness coefficient, λ_d, is the attraction coefficient between particles and the channel wall, characterizing the strength of particle deposition. The coefficients β_e and β_d determine the rate of erosion and deposition, respectively. According to (36), particle erosion and deposition also depend on the wall shear stress (WSS) τ, as well as the shear stress thresholds τ_e and τ_d, which in turn depend on the solid material properties at the channel interface. Erosion and deposition occur when WSS is larger and less than τ_e and τ_d, respectively. We calculate the range of these dimensionless parameters based on the dimensional quantities of the system under investigation.

TABLE I. Dimensional parameters for simulations [13,17,47,48].

Description	Symbol	Value
Porous medium thickness	D	$300\,\mu m$
Channel width	$2W$	0.1 to $1\,\mu m$
Viscosity	μ	$10^{-3}\,kg\,m^{-1}\,s^{-1}$
Initial pressure	P_{in}	600 to $1000\,kg\,m^{-1}\,s^{-2}$
Total density of the fluid and particles	ρ	$1000\,kg\,m^{-3}$
Diffusion coefficient	Ξ	10^{-12} to $10^{-7}\,m^2\,s^{-1}$
Typical particles concentration	C_{typ}	0–$1\,mol\,m^{-3}$
Particles concentration at the channel inlet	C_{in}	0–$1\,mol\,m^{-3}$
Erosion coefficient	Λ_e	10^{-12} to $2 \times 10^{-8}\,mol\,kg^{-1}\,m^{-1}\,s$
Stickiness coefficient	Λ_d	10^{-12} to $2 \times 10^{-8}\,m\,s^{-1}$
Erosion shear threshold	Σ_e	0–$100\,kg\,m^{-1}\,s^{-2}$
Deposition shear threshold	Σ_d	0–$100\,kg\,m^{-1}\,s^{-2}$
Erosion coefficient	B_e	10^{-8} to $6.25 \times 10^{-5}\,kg^{-1}\,m^2\,s$
Deposition coefficient	B_d	10^{-8} to $6.25 \times 10^{-5}\,mol^{-1}\,kg^{-1}\,m^5\,s$
Solid wall density	ρ_s	$1600\,kg\,m^{-3}$

TABLE II. Dimensionless parameters for simulations [13,17,47].

Description	Symbol/Formula	Value
Péclet number	$\mathrm{Pe} = \frac{W^2 P_{\mathrm{in}}}{\mu \Xi}$	0–50 000
Erosion coefficient	$\lambda_e = \frac{\Lambda_e \mu D}{2W^2 C_{\mathrm{typ}}}$	0–3
Stickiness coefficient	$\lambda_d = \frac{\Lambda_d \mu D^2}{W^3 P_{\mathrm{in}}}$	0–3
Erosion shear threshold	$\tau_e = \frac{2D\Sigma_e}{W P_{\mathrm{in}}}$	0–10
Deposition shear threshold	$\tau_d = \frac{2D\Sigma_d}{W P_{\mathrm{in}}}$	0–10
Erosion coefficient	$\beta_e = \frac{\rho_s B_e \mu}{2\rho W}$	0–1
Deposition coefficient	$\beta_d = \frac{\rho_s B_d \mu C_{\mathrm{typ}}}{2\rho W}$	0–1

We choose dimensional parameters as reported by Bonelli *et al.* [17]. Other parameters in our model are calculated based on quantities reported by other researchers [13,47,48].

Our numerical scheme is straightforward, based on second-order accurate finite-difference spatial discretization of the governing equations with explicit time stepping of the channel evolution for (33) and (36), respectively. We also use the trapezoidal quadrature to evaluate the integrals in (24) and (26). We organize our investigation of erosion and deposition in a channel as follows: First, the simulations are conducted under an erosion-only regime in Sec. IV A. We then analyze our model for the deposition scenario in Sec. IV B. Finally, we simultaneously investigate erosion and deposition in Sec. IV C. For the first two cases, we compare our results with experimental literature [13,17] in Sec. IV A 1 and Sec. IV B 1.

A. Validation of erosion

In this section we first compare our erosion model with the results developed by Bonnelli *et al.* [17] in Sec. IV A 1. Then we investigate the effects of the dimensionless erosion threshold τ_e and the dimensionless erosion rate coefficient β on the channel evolution in Sec. IV A 2 and Sec. IV A 3, respectively [17].

1. Channel evolution, comparison to experiments

Matching the erosion parameters when comparing our erosion model with the experimental works is challenging. Many studies have taken a conventional approach to validate the constitutive erosion model using the "hole erosion test" experiment. The experiment consists of flowing water through a cylindrical pipe made of a specific material of which the physical properties are known. Several parameters are extrapolated to study the pipe expansion during this test, undergoing a constant pressure-drop-driven flow. Bonnelli *et al.* [17] developed an analytical law based on the experiment to predict the expansion of a pipe given specific solid interface properties. They discovered a closed-form formula for the evolution of the dimensional channel radius $A(T)$ in terms of the pressure difference between the inlet and outlet of the channel $P_{\mathrm{in}} - P_{\mathrm{out}}$, the critical erosion threshold Σ_e, and the characteristic erosion time T_{er}:

$$\frac{A(T)}{A_{\mathrm{in}}} = 1 + \left(1 - \frac{2D\Sigma_e}{A_{\mathrm{in}}(P_{\mathrm{in}} - P_{\mathrm{out}})}\right)\left[\exp\left(\frac{T}{T_{\mathrm{er}}}\right) - 1\right]. \qquad (38)$$

Here D is the length of the channel, A_{in} is initial channel radius, and T_{er} is given by

$$T_{\mathrm{er}} = \frac{2D\rho_s}{(P_{\mathrm{in}} - P_{\mathrm{out}})\kappa_{\mathrm{er}}}, \qquad (39)$$

where ρ_s and κ_{er} (m^{-1} s) are the solid wall density and the erosion coefficient, respectively. The dimensional erosion coefficient B_e, appearing in our model in (12), is related to the erosion
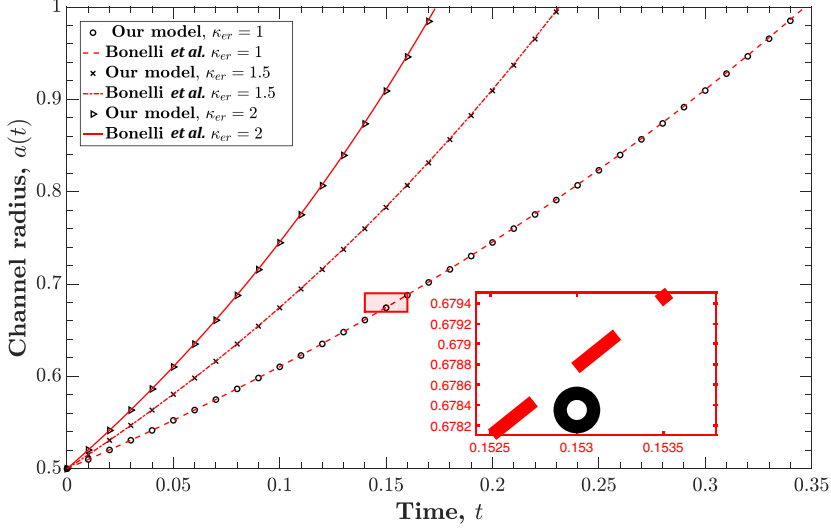
FIG. 3. Channel erosion: comparison of the channel radius $a(t)$ vs time t, based on our model and the dimensionless version of model proposed by Bonnelli *et al.* [17] given in (36) and (38), respectively, for three dimensionless erosion coefficients κ_{er}. The following parameters are used: $W = 0.5$ μm, $\rho = 1000$ kg m^{-3}, $\rho_s = 1600$ kg m^{-3}, $\Sigma_e = 0$ kg m^{-1} s^{-2}, $\Sigma_d = 0$ kg m^{-1} s^{-2}, $P_{\mathrm{in}} - P_{\mathrm{out}} = 10$ kg m^{-1} s^{-2}, and $B_d = 0$ mol^{-1} kg^{-1} m^5 s. For all simulations, the corresponding dimensionless parameters are $\tau_e = 0$, $\tau_d = 0$, $\beta_e = 1, 1.5, 2$ [$\beta_e = \kappa_{\mathrm{er}} \mu / (2\rho W)$], $\beta_d = 0$, and $a_{\mathrm{in}} = 0.5$.

coefficient κ_{er} by

$$B_e = \frac{\kappa_{\mathrm{er}}}{\rho_s}; \tag{40}$$

therefore we have $\beta_e = \kappa_{\mathrm{er}} \mu / (2\rho W)$ by using Table II. Here we set $B_e = 10^{-6}$ (kg^{-1} m^2 s), which is notably used for modeling purposes. The pipe erosion law given in (38) and derived by Bonnelli *et al.* [17] shows good compliance with the "hole erosion" experiment and is analytically exact for slow erosion. This closed-form formula has been widely used by researchers to validate their analytical and numerical approaches; for instance, Jägger *et al.* [13], who used a LBM to model erosion and deposition numerically. The parameters used to compare our model given in (36) with (38) proposed by Bonnelli *et al.* [17] are the initial channel radius of $A_{\mathrm{in}} = 0.5$ μm, the channel length $D = 300$ μm, $\kappa_{\mathrm{er}} = 1$–2 m^{-1}s, $\rho_s = 1600$ kg m^{-3}, and a pressure difference of $P_{\mathrm{in}} - P_{\mathrm{out}} = 10$ kg m^{-1} s^{-2}. In order to allow maximum erosion, we set the erosion threshold $\Sigma_e = 0$ in both our model in (12) [i.e., the Heaviside function in (36) is continuously equal to one] and the exponential law in (38). We use the same parameters to evaluate and compare our model with the experiment. In Fig. 3 we compare our model given in (36) with the exponential law expression given in (38) for several values of the dimensional erosion coefficient κ_{er}. Our model shows good agreement with the model given in (38) proposed by Bonnelli *et al.* [17]. We note the discrepancy observed in the validation of our model with that of Bonnelli *et al.* [17], notably for the simulation with $\kappa_{\mathrm{er}} = 1$ as showcased in Fig. 3. We note that the black markers, corresponding to our simulation, are produced by the forward Euler discretization of the temporal term in (36). Setting $\tau_e = 0$, we obtain

$$\frac{a^{n+1} - a^n}{\Delta t} = \beta_e a^n \Rightarrow a^{n+1} = (1 + \beta_e \Delta t) a^n, \tag{41}$$
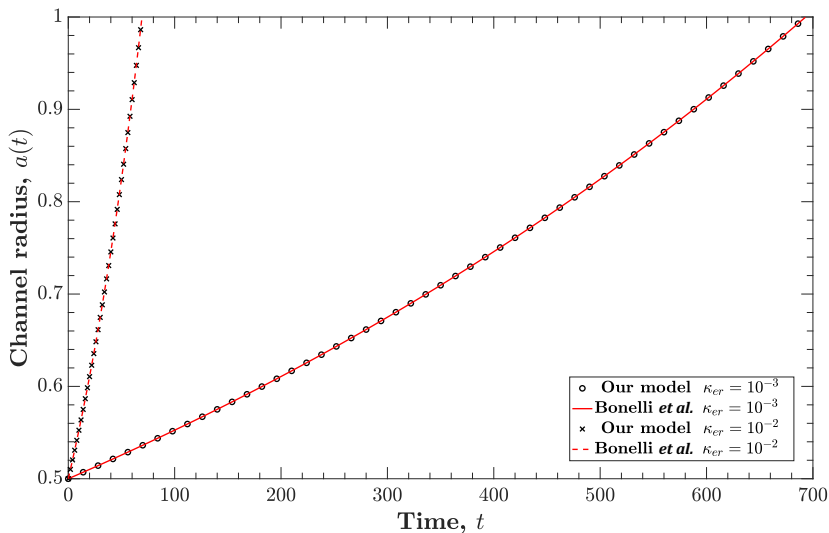
FIG. 4. Channel erosion: comparison of the channel radius $a(t)$ vs time t, based on our model and the dimensionless version of model proposed by Bonnelli *et al.* [17] given in (36) and (38), respectively, for two dimensionless erosion coefficients κ_{er}. The following parameters are used: $W = 0.5$ µm, $\rho = 1000$ kg m^{-3}, $\rho_s = 1600$ kg m^{-3}, $\Sigma_e = 0$ kg m^{-1} s^{-2}, $\Sigma_d = 0$ kg m^{-1} s^{-2}, $P_{in} - P_{out} = 10$ kg m^{-1} s^{-2}, and $B_d = 0$ mol^{-1} kg^{-1} m^5 s. For all simulations, the corresponding dimensionless parameters are $\tau_e = 0$, $\tau_d = 0$, $\beta_e = 0.001, 0.01$ [$\beta_e = \kappa_{er}\mu/(2\rho W)$], $\beta_d = 0$, and $a_{in} = 0.5$.

where $a^n = a(n\Delta t)$. Hence, it can easily be shown that the forward Euler approximation takes the form of

$$a^n = (1 + \beta_e \Delta t)^n a^0. \tag{42}$$

Since the exact solution is given by the following, letting $t^n = n\Delta t$:

$$a(t^n) = e^{\beta t^n} a_0 = e^{n\Delta t\beta} a_0 = (e^{\Delta t\beta})^n a_0. \tag{43}$$

Therefore, we see that the forward Euler scheme approximates the exponential term $e^{\Delta t\beta} \approx 1 + \beta\Delta t$, and the error is of $O[(\beta\Delta t)^2]$, explaining the discrepancy in Fig. 3. Notably, the forward Euler discretization with specific time steps introduces some error in approximating the exponential law derived by Bonnelli *et al.* [17]. Of course, such a discrepancy could be overcome by using a finer temporal mesh.

When setting the erosion coefficient to the reference values in Bonnelli's work [31], i.e., 10^{-3}–10^{-2}, the erosion process exhibits slow dynamics, particularly when coupled with a deposition term. Therefore, the order of magnitude of our parameter selection is based on the work by Jägger *et al.* [13], which is more pertinent to our study as it incorporates both erosion and deposition. In their research, Jägger *et al.* [13] utilized the parameter κ_{er} within the range of 0.05 to 1. To underscore that our choice of parameters is a deliberate modeling decision rather than a reflection of the model's validity, we run a simulation replicating the erosion validation plot using the parameters from Bonelli's work. In Fig. 4, we vary the parameter κ_{er} from 10^{-3} to 10^{-2}. The observed trend reveals a significantly prolonged time required for complete erosion compared to Fig. 3. This outcome aligns with the findings presented in Sec. IV A 3, notably that the erosion coefficient is responsible for the time at which the complete erosion of the channel occurs.

Next, we validate our model against the work proposed by Bonelli *et al.* [17] for the dimensional erosion threshold, Σ_e. It is noteworthy that Σ_e is directly related to the dimensionless erosion threshold, denoted as $\tau_e = \frac{2D\Sigma_e}{WP_{in}}$. While keeping the erosion coefficient κ_{er} fixed at 8, we conduct
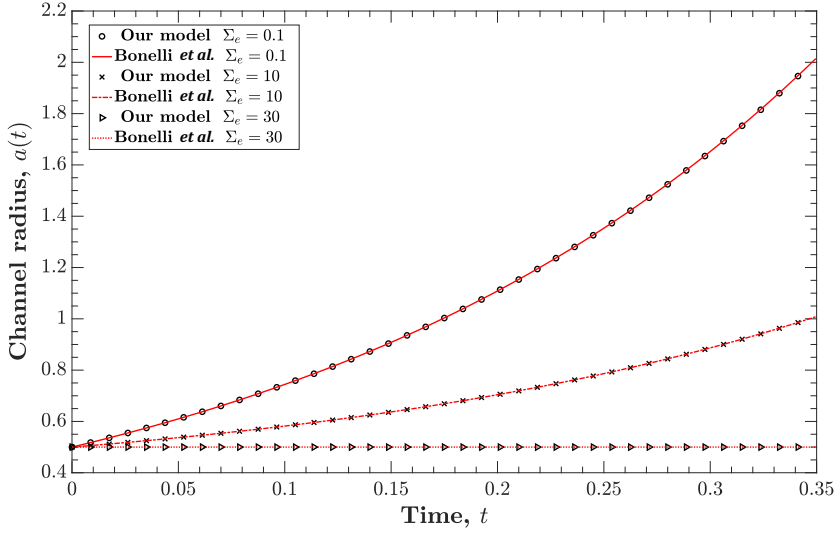
FIG. 5. Channel erosion: comparison of the channel radius $a(t)$ vs time t, based on our model and the dimensionless version of model proposed by Bonnelli et al. [17] given in (36) and (38), respectively, for three dimensionless erosion thresholds Σ_e. The following parameters are used: $W = 0.5$ μm, $\rho = 1000$ kg m^{-3}, $\rho_s = 1600$ kg m^{-3}, $\kappa_{er} = 4$ m^{-1}s, $\Sigma_d = 0$ kg m^{-1} s^{-2}, $P_{in} - P_{out} = 10$ kg m^{-1} s^{-2}, and $B_d = 0$ mol^{-1} kg^{-1} m^5 s. For all simulations, the corresponding dimensionless parameters are $\tau_d = 0$, $\tau_e = 0.0017, 0.1667, 0.5$, $(\beta_e = 8)$, $\beta_d = 0$, and $a_{in} = 0.5$.

simulations with varying parameters, specifically for $\Sigma_e = 0.1, 10, 30$. The comparison between our model and that of Bonelli et al. [17] is presented in Fig. 5, illustrating a good agreement between the two approaches. We point to the linear and nonlinear growth of the channels as a function of time and attempt to present an intuitive picture behind this phenomenon. Equation (36) suggests that the radius profile under an erosion-only regime evolves as

$$\frac{\partial a}{\partial t} = \beta_e(\tau - \tau_e)h|_{\tau_0 - \tau_e}. \tag{44}$$

Again, assuming a cylindrical channel which widens uniformly across time, the shear stress is equal to the radius profile as $\tau(t) = a(t)$. Letting $\tau_e < \tau$, we obtain

$$\frac{\partial a}{\partial t} = \beta_e(a - \tau_e), \tag{45}$$

which admits an analytical solution after integrating both sides:

$$a = (a_0 - \tau_e)e^{\beta t} + \tau_e. \tag{46}$$

The expression, although written differently, agrees with the model presented by Bonelli et al. [17], i.e., (38). Moreover, Taylor expansion of the exponential term in the expression above about $t = 0$, yields

$$a = (a_0 - \tau_e)\left[1 + \beta_e t + (\beta_e t)^2 + O(\beta_e^3 t^3)\right] + \tau_e \Rightarrow a = a_0 + \beta_e(a_0 - \tau_e)t + (a_0 - \tau_e)\beta_e^2 t^2. \tag{47}$$

Several insights can be derived from the form above:

(1) If $a_0 = \tau_e$, then the channel does not erode, a scenario illustrated in Fig. 5, where the erosion threshold τ_e is set to 0.5, corresponding to the initial radius of the channel.

(2) At the beginning of the simulation, that is for $t \approx 0$, the growth is linear, as can be seen by the validation figures, i.e., Figs. 3–5.
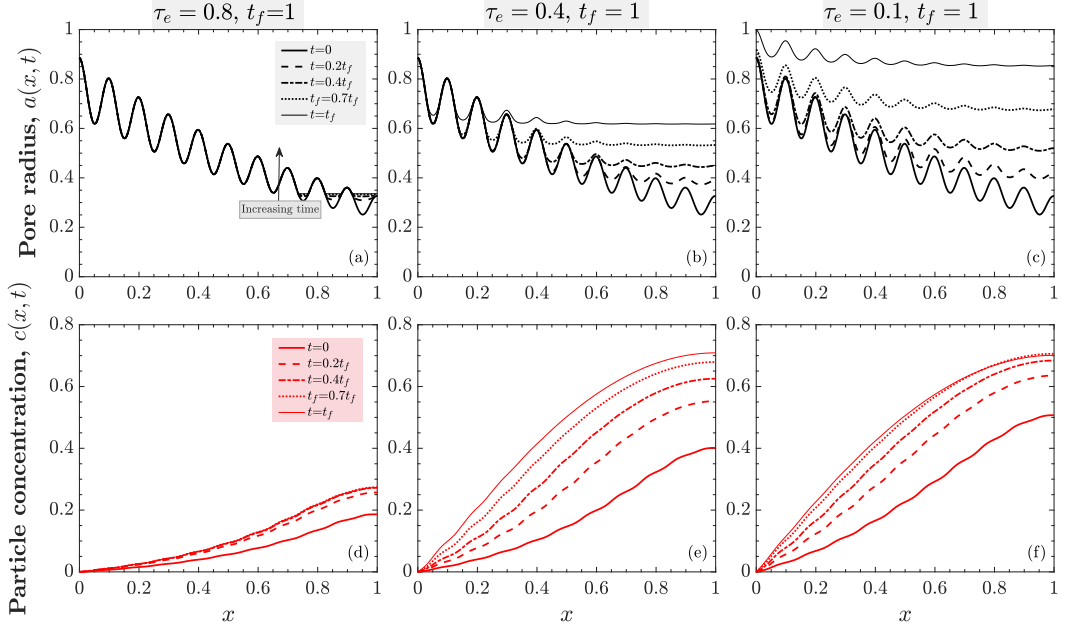
FIG. 6. Channel radius evolution $a(x,t)$ [black curves in (a)–(c)] and the particle concentration profile $c(x,t)$ [red curves in (d)–(f)], at several different times, for three different erosion shear stress thresholds τ_e with their corresponding erosion coefficients λ_e: $\tau_e = 0.8$ and $\lambda_e = 0.6$; $\tau_e = 0.4$ and $\lambda_e = 0.3$; and $\tau_e = 0.1$ and $\lambda_e = 0.075$. For all simulations, the following parameters are used: Pe = 2, $\alpha_e = 0.75$, $\alpha_d = 0.75$ $\lambda_d = 0$, $\tau_d = 0$, $\beta_e = 1$, $\beta_d = 0$, $c_{in} = 0$, and $a_{in} = \frac{0.65}{0.55}(\frac{6.5 + \cos(20\pi x)}{10})e^{-x}$.

(3) When $\beta_e \ll 1$, then the growth is linear. That is the second-order temporal term in the expression above [see (47)] vanishes, yielding a linear growth: $a = a_0 + \beta_e(a_0 - \tau_e)t$. Of course, the erosion would be much slower, since the only terms contributing to erosion are linear in time.

2. Effects of erosion shear threshold τ_e

In this section, we present a parametric study of the effect of the shear stress threshold τ_e on the channel evolution and particle concentration within the channel. We set the deposition shear stress threshold $\tau_d = 0$, the stickiness coefficient $\lambda_d = 0$, and the inlet particle concentration $c_{in} = 0$ in order to have an erosion-only model. We fix the erosion coefficient $\beta_e = 1$ and consider the initial channel profile as a cosine function to be able to capture the effects of shear stress on the channel erosion. The initial channel profile is given in the caption of Fig. 6. Figures 6(a)–6(c) show the pore evolution $a(x,t)$ vs x and Figs. 6(d)–6(f) represent the corresponding particle concentration evolution $c(x,t)$ for several values of τ_e equal to 0.8, 0.4, and 0.1, respectively, at various times throughout the erosion process. Here the final time $t_f = 1$, which is the time that we stop the simulation or it might be the time that the channel radius at any cross section becomes 1, or equivalently the channel expands up to the lattice border. The variation of the shear threshold τ_e, clearly affects the shape of the final radius profile of the channel and the maximum erosion depth. For a low shear threshold $\tau_e = 0.1$, the entire surface along the channel length erodes. We notice that the significant enlargement of the channel occurs first towards the channel outlet. Since the initial channel radius decreases with the channel depth, WWS has a larger magnitude towards the channel outlet, leading to higher downstream erosion. For higher values of τ_e, as shown in Figs. 6(a) and 6(b), erosion is less pronounced [compared to Fig. 6(c), where τ_e has a lower value] and occurs only at the downstream side of the channel, preventing the channel from attaining a uniform final shape.
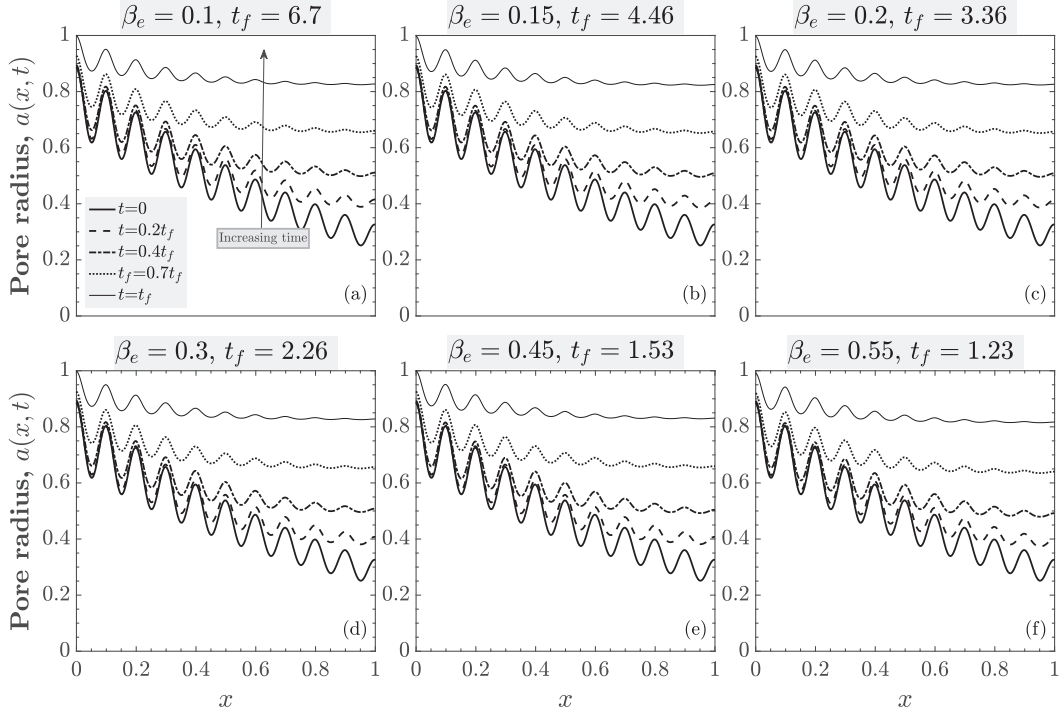
FIG. 7. Channel radius evolution $a(x, t)$ vs x, for several different erosion coefficients β_e. For all simulations, the following parameters are considered: Pe $= 2$, $\alpha_e = \alpha_d = 0.75$, $\lambda_e = 0.0375$, $\lambda_d = 0$, $\tau_e = 0.05$, $\tau_d = 0$, $\beta_d = 0$, $c_{\text{in}} = 0$, and $a_{\text{in}} = \frac{0.65}{0.55}(\frac{6.5 + \cos(20\pi x)}{10})e^{-x}$.

Mathematically, this is due to the presence of the Heaviside function in (36), leading to erosion occurring at the locations with higher shear stress τ than the erosion threshold τ_e.

As mentioned earlier, Figs. 6(d)–6(f) show the particle concentration evolution vs x for several values of τ_e at various times. Particles are eroded at the wall of the channel and transported by the flow; therefore, the particle concentration increases along the channel depth. This process is depicted in Figs. 6(d)–6(f), where there is a higher concentration of particles, compared to the inlet region, at the channel downstream. Our results show that the particle concentration in the channel is higher for lower shear stress threshold τ_e. Since less erosion occurs when $\tau_e = 0.8$, we observe fewer particles are accumulated at the channel outlet as shown in Fig. 6(d). Conversely, the particle concentration profile increases throughout the channel for smaller values of τ_e because more particles get torn from the channel wall and are carried away by the flow, resulting in a high concentration at the channel downstream. Depending on the transport regime desired or depicted, the shear threshold is related to the channel wall properties, and the initial channel geometry is a metric to control the erodibility and, thus, the final configuration of the channel.

3. Effects of erosion coefficient β_e

Figures 7(a)–7(f) illustrate the channel radius $a(x, t)$ vs x, for several values of the erosion coefficient β_e. As shown in these figures, the variation of β_e affects the final time t_f, which is here representing the time that the channel radius at any cross section becomes 1, or equivalently the channel expands up to the lattice border. The final channel configuration is similar in all simulations; however, the only difference is the final time to reach such configurations. For a relatively small erosion coefficient $\beta_e = 0.1$, it takes a dimensionless time of $t_f = 6.7$ for the channel to be completely eroded. Alternatively, increasing the erosion coefficient to $\beta_e = 0.55$ shows that it takes

a dimensionless time of $t_f = 1.23$ to reach a similar final configuration. The variation of the erosion coefficient β_e attests to the fact that, for the same threshold shear stress threshold $\tau_e = 0.05$ (used in this simulation), the final time to reach the stabilized state is not practically equal. Incrementing β_e in Figs. 6(a)–6(f) results in shorter times to attain a complete erosion; therefore, the erosion coefficient governs the rate at which erosion occurs. As noted in Sec. IV A 2, the final erosion configuration depends on the shear stress threshold τ_e, and according to Figs. 7(a)–7(f) the rate at which such configurations are attained is specified by the erosion coefficient β_e.

B. Validation of depositon

In this section we first compare our deposition model with the results developed by Jäger *et al.* [13] in Sec. IV B 1. Then we investigate the effects of the dimensionless deposition threshold τ_d on the channel evolution in Sec. IV B 2.

1. Channel evolution, comparison to experiments

As reported by Jäger *et al.* [13], the dimensional porous medium channel radius $A(T)$ evolves with time T due to particle deposition and can be obtained by

$$\frac{A(T)}{A_{\text{in}}} = 1 + \left(1 - \frac{2D\Sigma_d}{A_{\text{in}}(P_{\text{in}} - P_{\text{out}})}\right)\left[\exp\left(\frac{T}{T_{\text{dep}}}\right) - 1\right], \tag{48}$$

where $T_{\text{dep}} = 2\rho D/(C\kappa_{\text{dep}}P_{\text{in}})$ is the characteristic deposition time scale, and C the concentration of particles along the pore. Note that $\kappa_{\text{dep}} = \rho_s B_d$, which is the dimensional deposition coefficient used by Jäger *et al.* [13] and is related to the dimensional deposition coefficient B_d [see (12)]. To validate our deposition model, we set the dimensionless deposition shear stress threshold τ_d, larger than WWS τ, to allow complete deposition; i.e., the Heaviside function in (36) is continuously equal to one. Since the deposition law (48) does not account for the concentration of particles variation along the channel axis, we consider a constant dimensionless concentration of particles $c = 1$ in (36); hence we neglect the changes of the particles concentration along the channel captured by the effect of the advection-diffusion equation (33). Figure 8 shows a good agreement between the dimensionless version of deposition law (48) and our dimensionless deposition model (36) for different values of deposition coefficient $\beta_d = \frac{\kappa_{\text{dep}}\mu C_{\text{typ}}}{2\rho W}$ (see also Table II), which confirms the validity of our model. Next, we validate our model against the work proposed by Jäger *et al.* [13] for the dimensional deposition threshold, Σ_d. We recall that Σ_d is directly related to the dimensionless deposition threshold, denoted as $\tau_d = \frac{2D\Sigma_d}{WP_{\text{in}}}$. While keeping the deposition coefficient κ_{dep} fixed at 10, we conduct simulations with varying parameters, specifically for $\Sigma_d = 10, 20, 40$. The comparison between our model and that of Jäger *et al.* is presented in Fig. 9, illustrating a good agreement between the two approaches.

2. Variation of deposition shear threshold τ_d

To understand the effect of the deposition shear threshold τ_d, we consider a setup consisting of fixed values of Péclet number Pe = 2; erosion coefficient $\beta_e = 0$ and erosion threshold $\tau_e = 0$; and stickiness coefficient $\lambda_d = 2$. We simulate the channel radius evolution for three different deposition thresholds: $\tau_d = 0.4$, $\tau_d = 0.6$, $\tau_d = 0.9$, as shown in Figs. 10(a), 10(b), and 10(c), respectively. For a relatively low deposition threshold in Fig. 10(a), we observe a slight deposition of particles at the channel inlet. As τ_d increases in Figs. 10(b) and 10(c), we observe more deposition occurring along the channel. These can also be confirmed in Figs. 10(d)–10(f) as the particle concentration at the channel outlet is lower compared to the rest of the channel. In addition, the particle concentration decreases as τ_d increases in Figs. 10(d)–10(f).
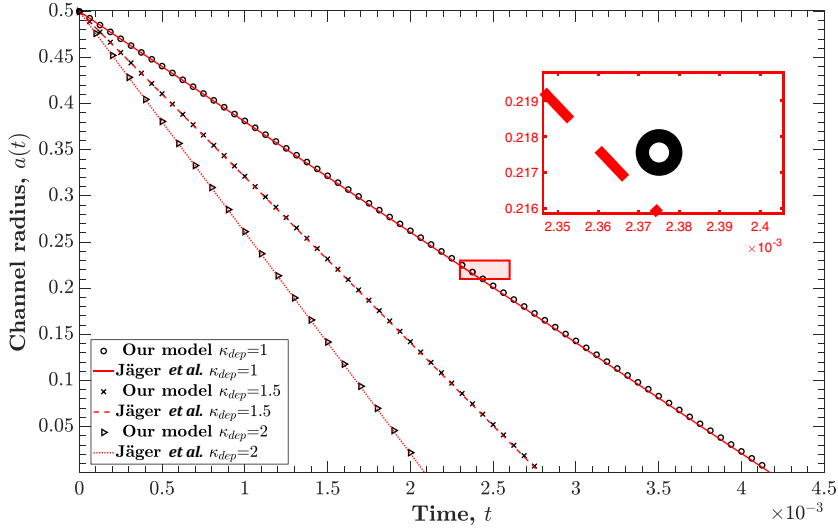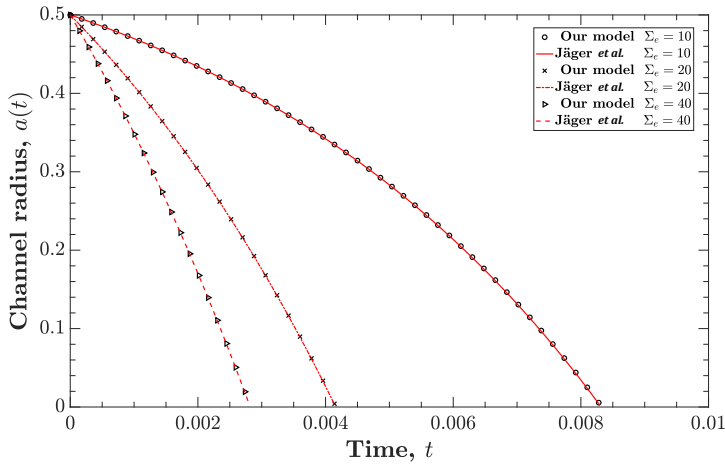
FIG. 8. Channel deposition: comparison of the channel radius $a(t)$ vs time t, based on our model and the dimensionless version of model proposed by Jäger *et al.* [13] given in (36) and (48), respectively, for three dimensionless deposition coefficients κ_{dep}. The following parameters are used: $W = 0.5$ μm, $\rho = 1000$ kg m^{-3}, $\rho_s = 1600$ kg m^{-3}, $\Sigma_e = 0$ kg m^{-1} s^{-2}, $\Sigma_d = 0.4$ kg m^{-1} s^{-2}, $P_{\mathrm{in}} - P_{\mathrm{out}} = 10$ kg m^{-1} s^{-2}, and $B_e = 0$ kg^{-1} m^2 s. For all simulations, the corresponding dimensionless parameters are $\tau_e = 0$, $\tau_d = 24$, $\beta_e = 0$, $\beta_d = 1, 1.5, 2$ [$\beta_d = \kappa_{\mathrm{dep}} \mu C_{\mathrm{typ}}/(2\rho W)$], and $a_{\mathrm{in}} = 0.5$. The deposition coefficient in Jäger *et al.* [13], κ_{dep}, is related to deposition coefficient in our model, B_d, via $\kappa_{\mathrm{dep}} = \rho_s B_d$.

FIG. 9. Channel deposition: comparison of the channel radius $a(t)$ vs time t, based on our model and the dimensionless version of model proposed by Jäger *et al.* [13] given in (36) and (48), respectively, for three deposition threshold coefficients Σ_d. The following parameters are used: $W = 0.5$ μm, $\rho = 1000$ kg m^{-3}, $\rho_s = 1600$ kg m^{-3}, $\Sigma_e = 0$ kg m^{-1} s^{-2}, $\kappa_{\mathrm{dep}} = 10$ m^{-1} s, $P_{\mathrm{in}} - P_{\mathrm{out}} = 10$ kg m^{-1} s^{-2}, and $B_e = 0$ kg^{-1} m^2 s. For all simulations, the corresponding dimensionless parameters are $\tau_e = 0$, $\tau_d = 0.1667, 0.3333, 0.6667$, $\beta_e = 0$, $\beta_d = 2$, and $a_{\mathrm{in}} = 0.5$. The deposition coefficient in Jäger *et al.* [13], κ_{dep}, is related to deposition coefficient in our model, B_d, via $\kappa_{\mathrm{dep}} = \rho_s B_d$.
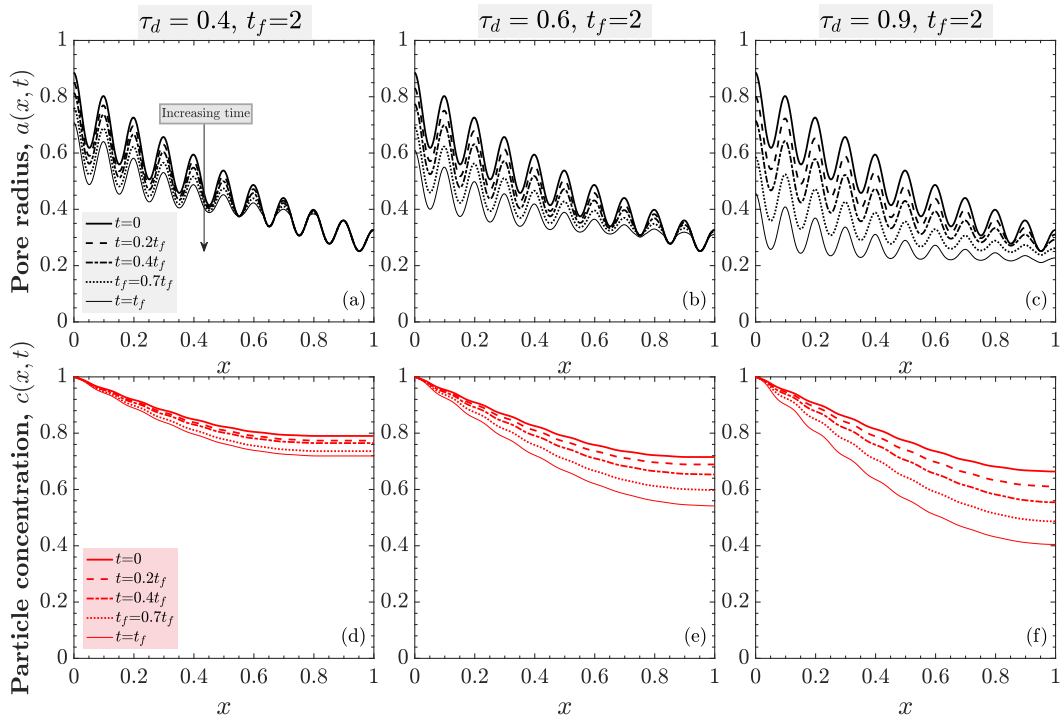
FIG. 10. Illustration of the pore radius evolution $a(x,t)$ (black curves) and its respective particles concentration profile $c(x,t)$ (red curves), at several different times, and for three different deposition shear stress thresholds τ_d and their corresponding stickiness coefficients λ_d: (a) and (d) $\tau_d = 0.4$ and $\lambda_d = 0.4$, (b) and (e) $\tau_d = 0.6$ and $\lambda_d = 0.45$, (c) and (f) $\tau_d = 0.9$ and $\lambda_d = 0.675$. For all simulations, the following parameters and initial channel profile are considered: $\tau_e = 2$ (high enough to cancel erosion), Pe = 2, $\alpha_e = 0.75$, $\alpha_d = 0.75$, $\lambda_e = 1.5$, $\beta_e = 0$, $\beta_d = 0.5$, $c_{\text{in}} = 0.5$, $a_{\text{in}} = \frac{0.65}{0.55}\left(\frac{6.5 + \cos(20\pi x)}{10}\right)e^{-x}$.

C. Channel with active erosion and deposition

In the previous sections, we simulated each erosion and deposition solely and investigated the influence of the governing parameters, notably τ_e and β_e for erosion and τ_d and β_d for deposition. We now simulate our model in a channel setting with both active erosion and deposition occurring simultaneously. As before, our interpretation is based on the erosion law (36), which considers the rate of erosion and deposition as a function of the shear stress exerted on the channel wall. Two main components of erosion and deposition characterize this law, notably τ_e and τ_d. When the shear stress exerted by the fluid flow at the channel wall is large or low enough to generate the erosion or deposition processes, respectively, the channel cross section responds either by losing or absorbing particles, which are then transported to the channel downstream or deposited on the channel wall, respectively. The alternation of both processes within the scope of the threshold law results in channel reconfiguration. In this section, our modeling efforts aim to characterize the occurrence of erosion and deposition simultaneously and, therefore, classify them within their respective parameters regimes.

1. Sensitivity to the erosion and deposition thresholds

For the following simulations, we impose a variation of the threshold coefficients τ_e and τ_d, which affect the channel's overall performance in response to the fluid flow forces. Here we consider the change of the channel volume defined by $\Delta V = \int_0^1 [a^2(x, t_f) - a^2(x, 0)] \, dx$, as a metric to classify
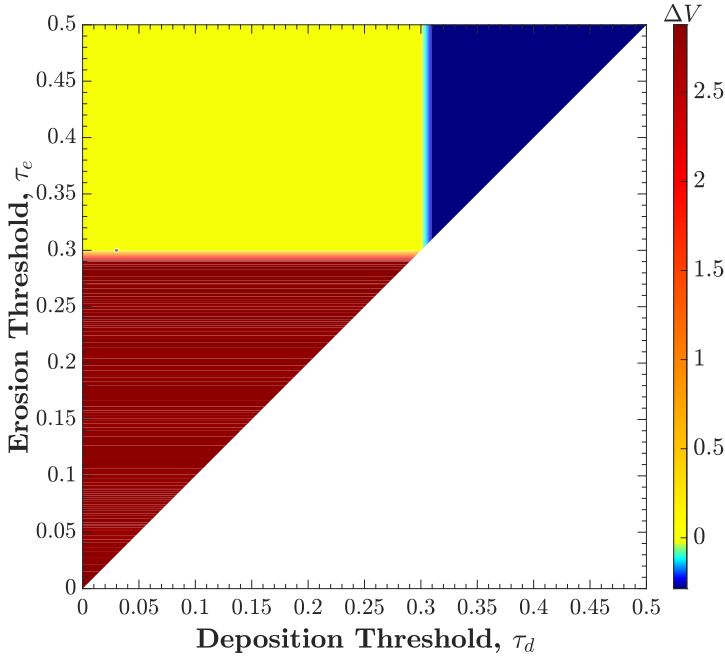
FIG. 11. Illustration of the channel volume change, $\Delta V = \int_0^1 (a^2(x, t_f) - a^2(x, 0)) \mathrm{d}x$, in terms of a parametric study of the shear stress thresholds τ_e and τ_d. The following parameters and initial channel profile are considered: Pe $= 2$, $\alpha_e = \alpha_d = 0.75$, $\lambda_e = 0.4$, $\lambda_d = 0.4$, $\beta_e = 0.3$, $\beta_d = 0.3$, $c_{\mathrm{in}} = 1$, and $a_{\mathrm{in}} = 0.3$.

the flow and solid transport regime, which is simply the difference between the final and initial channel volumes. Note that positive ΔV denotes the presence of erosion; hence the channel expands over time. Alternatively, negative ΔV depicts the presence of particle deposition, where the channel is subject to clogging eventually. Here we use a set of parameters τ_e and τ_d ranging from 0–0.5, as well as an initial concentration of $c_{\mathrm{in}} = 1$. To examine the combined impact of the imposed shear stress thresholds, we first consider a simple channel geometry, where $a(x, 0) = a_{\mathrm{in}} = 0.3$. This initial geometry leads to an initial shear stress distribution of $\tau(x, 0) = 0.3$, according to (26). Theoretically, our shear stress law (36) describes three potential scenarios: (1) solely erosion regime, if $\tau(x, 0) = 0.3 \geqslant \tau_e > \tau_d$, (2) deposition-only scenario, if $\tau_e > \tau_d \geqslant \tau(x, 0) = 0.3$, and (3) static model in which no change occurs within the pore, if $\tau_e > \tau(x, 0) = 0.3 > \tau_d$. To demonstrate these, in Fig. 11, we plot the change in pore volume ΔV for τ_e and τ_d values ranging from 0 to 0.5. The red region represents complete erosion and occurs when $\tau(x, 0) = 0.3 \geqslant \tau_e > \tau_d$. The blue region, representing negative ΔV, is observed for $\tau_e > \tau_d \geqslant \tau(x, 0) = 0.3$. Finally, the yellow region shows $\Delta V = 0$, when $\tau_e > \tau(x, 0) = 0.3 > \tau_d$.

As discussed earlier, it is important to study channels with more complex initial geometries in real-world scenarios. Figure 12(a) represents a contour plot that depicts the change in channel volume as a function of the erosion and deposition thresholds for a complex initial geometry $a_{\mathrm{in}} = \frac{0.65}{0.55}(\frac{6.5 + \cos(20\pi x)}{10})e^{-x}$ and an initial particle concentration of $c_{\mathrm{in}} = 1$. The initial shear stress profile is not constant across the depth of the channel and varies with the depth x according to (26). As a result, the shear stress is lower near the channel inlet, where the channel radius is relatively wider. Conversely, the shear stress is higher near the channel outlet, where the channel radius is relatively narrower. Despite this complex structure of the initial shear stress, the three different regions can still be observed, as indicated by the colored regions red, blue, and yellow, similar to Fig. 11. As previously noted, the red region denotes areas of high erosion, where channels characterized by material properties of τ_e and τ_d undergo substantial erosion, resulting in a positive volume change,
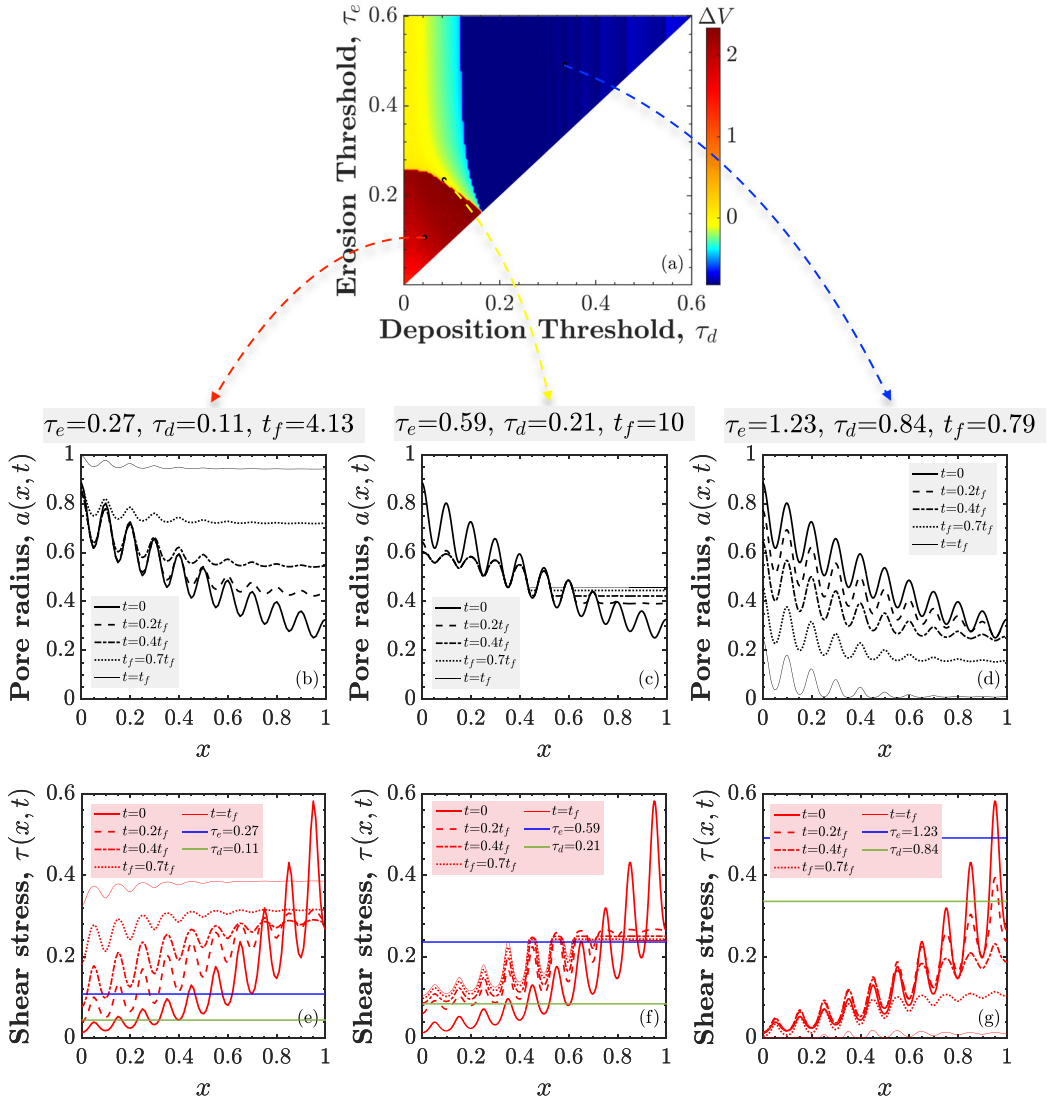
FIG. 12. (a): Illustration of the volume change, $\Delta V = \int_0^1 [a^2(x, t_f) - a^2(x, 0)]dx$, of the channel in terms of a parametric study of the shear threshold values τ_e and τ_d, with an initial concentration at the channel inlet $c_{\text{in}} = 0.3$. The channel pore radius evolution $a(x, t)$ [black curves in (b)–(d)] and its respective shear stress profile evolution $\tau(x, t)$ [red curves in (e)–(g)] are simulated for three pairs of shear threshold values: in (b) and (e) $\tau_e = 0.27$, $\tau_d = 0.11$, in (c) and (f) $\tau_e = 0.59$, $\tau_d = 0.21$, in (d) and (g) $\tau_e = 1.23$, $\tau_d = 0.84$. For all simulations, the following parameters are considered: Pe = 2, $\alpha_e = \alpha_d = 0.75$, $\lambda_e = 0.4$, $\lambda_d = 0.4$, $\beta_e = 0.3$, $\beta_d = 0.3$, and $a_{\text{in}} = \frac{0.65}{0.55}(\frac{6.5 + \cos(20\pi x)}{10})e^{-x}$.

$\Delta V > 0$. Conversely, channels falling within the yellow region, with τ_e and τ_d values, exhibit $\Delta V = 0$, indicating that they are either resistant to shear stress forces and experience neither erosion nor clogging or undergo both erosion and deposition equally. Finally, channels characterized by τ_d and τ_e within the blue region experience significant deposition, resulting in a negative volume change ($\Delta V < 0$), ultimately leading to clogging.

To further validate our understanding of the three distinct regions and to gain a deeper insight into the processes occurring in each, we select three different pairs of threshold values τ_e and τ_d, and plot the evolution of the pore radius profile at various time instances, as shown in Figs. 12(b), 12(c), and 12(d). For the pair of values $\tau_e = 0.27$ and $\tau_d = 0.11$, which lies within the red region of the contour plot, we observed significant erosion of particles, which leads to a substantial widening of the pore. We should note that particle deposition also occurs at the start of the simulation, but its effect is comparatively minimal; for a detailed analysis; see the discussion below. Conversely, the channel is subject to complete deposition for the pair of values $\tau_e = 1.23$ and $\tau_d = 0.84$ in the blue region. For the pair of values $\tau_e = 0.59$ and $\tau_d = 0.21$, within the yellow region of the contour plot, we observe deposition at the inlet of the pore and erosion at the channel downstream. The amount of material deposited near the channel inlet is nearly equal to the amount of material eroded near the outlet, leading to an insignificant change in the pore volume.

Figures 12(e), 12(f), and 12(g), which are corresponding to Figs. 12(b), 12(c), and 12(d), respectively, help to delve deeper into the impact of the initial channel profile and the corresponding shear stress profile, as described by (26). Here the evolution of the pore radius and shear stress profiles are analyzed at different time instances. According to Figs. 12(b) and 12(e), the shear stress profile thresholds are shown by the blue and green lines, $\tau_e = 0.27$ and $\tau_d = 0.11$, and they are chosen from the red region of Fig. 12(a). As a result, most parts of the channel undergo complete erosion initially at $t = 0$. However, for the parts of the channel where the initial shear stress lies between the blue and green threshold lines, no erosion and deposition are observed during the early stages of the simulation. A slight deposition of particles can be seen near the inlet for the parts of the channel where the initial shear stress is below the deposition threshold, given by the green line. As the simulation progresses, the pore radius widens, and the corresponding shear stress profile evolves. The shear stress profile smoothens over time, with peak values becoming smaller, especially near the outlet region. On the other hand, near the inlet region, the shear stress increases monotonically over time. Ultimately, the smoothed shear stress profile exceeds the erosion threshold, τ_e, resulting in the complete erosion of the channel.

In Figs. 12(c) and 12(f), we used the threshold values selected from the yellow region of Fig. 12(a). The initial shear stress profile lies within all three regions of the contour plot. From the inlet to halfway through the channel, the shear stress is below the green threshold line, given by a value of $\tau_d = 0.21$, leading to the deposition of particles. In contrast, for a region approximately between $x = 0.5$ and $x = 0.75$, the shear stress is lower than the erosion threshold and greater than the deposition threshold (represented by the blue and green lines, respectively); hence no immediate erosion or deposition is observed until later stages of the simulation with minimal effect. The shear stress is higher than the erosion threshold at the channel outlet, resulting in considerable erosion. Over time, the shear stress converges to a profile between the blue and green lines, indicating a stable state where the pore does not undergo any further erosion or deposition.

In Figs. 12(d) and 12(g), we used the threshold values that are selected from the blue region of Fig. 12(a). As shown, for most of the channel, the initial shear stress profile lies below the deposition threshold τ_d, which leads to a complete deposition of the particles in the channel. However, near the outlet region, the shear stress is partially above the erosion threshold τ_e, causing a slight erosion, though so minimal that it is not visible in the plot. Additionally, there are regions near the outlet where the shear stress is greater than τ_d and less than τ_e, leading to a lack of occurrence of either deposition or erosion at the initial stage of the simulation, i.e., at $t = 0$ and $t = 0.2t_f$. As time evolves, the shear stress profile smoothes, leading to a profile that lies below the deposition threshold, resulting in a sharp deposition and eventually clogging of the channel.

V. CONCLUSION

This paper aims to study and model the erosion and deposition processes within a parametric framework using an asymptotically reduced one-dimensional model. We present a model combining the Stokes equations for the flow and an advection-diffusion equation for the solid transport in an

idealized porous medium consisting of an array of axisymmetric channels. We specifically focus on a channel as the results can be replicated in the same manner for the rest of the channels. Due to the erosion and deposition of particles, the channel interface evolves, which is captured by applying a threshold law. We have shown that the flow regime within a given channel depends on the game of parameters utilized in the simulation, which we obtain from the properties of the channel material as well as suspended particles in the flow. After evaluating the assumptions for simplification purposes and using asymptotic analysis, we note some parameters among which the flow regime responds by erosion or deposition. These parameters affect the channel final shape and configuration; when the pore bed cannot withstand the shear forces exerted by the flow, either erosion or deposition occurs at the channel cross section. We confirm and validate that our model can capture the interface evolution by comparing it with the scaling law extrapolated from the hole erosion test [31]. While we couldn't directly compare our erosion model with experiments due to the lack of available data, we did compare it with the analytical expression developed by Bonnelli *et al.* [17], which has been proven against experimental results. This limitation encourages us to collaborate with experimentalists in the future to bridge the gap between theory and experimental validation.

A parametric simulation is presented to classify erosion and deposition according to the imposed parameters. We investigated the effects of the shear stress thresholds, τ_e and τ_d, which affect the depth and final configuration of the temporal and spatial evolution, which are crucial in our erosion law. We also present the effects of the erosion coefficient β_e, which affects the rate/speed at which erosion occurs within the channel. Specifically, in Fig. 7, It is recorded that the final shape is visibly similar for all simulations with different erosion coefficients; however, the necessary time to attain such configuration varies. To understand the regime within the channel and its dependence on the unique game of parameters utilized, we present that three main regimes can be noted when evaluating the pore volume's overall change, as shown in Fig. 12(a):

(1) Erosion: τ_e and β_e affect the rate at which particles get torn away from the channel wall by the flow. The overall change in the channel volume ΔV is positive because the final configuration attains a wider shape within every cross section along the channel.

(2) Deposition: The deposition shear stress τ_d, highly affects the final configuration and rate at which particles deposit on the channel wall. In this case, ΔV is negative.

(3) Alternation of both erosion and deposition: As shown in the contour plot in Fig. 12(a), when the erosion and deposition parameters fall within the stagnation region ($\Delta V = 0$), two subregimes can occur:

(1) Erosion and deposition can happen simultaneously along the pore, compensating for the change in the volume; hence, the amount of the eroded particles is close to that of deposited, which results in a trivial change in the channel volume.

(2) The flow within the pore exerts shear stress less than the erosion and more than the deposition shear stress thresholds τ_e and τ_d, respectively. Therefore the channel interface does not undergo any reconfiguration and remains intact.

In developing our model, we made deliberate choices and simplifying assumptions to balance practical applicability with computational efficiency. By assuming a fluid in a dilute limit, we aim to develop a framework for practitioners and experimentalists. Although the inclusion of four-way couplings could provide a more comprehensive depiction of the particle-particle collisions and fluid-particle interactions, our focus on simplicity and accessibility allowed for a fast computational process. Notably, the model's ability to yield rapid results, even under the assumption of dilute suspensions, proved advantageous for obtaining analytical insights into pore behavior during erosion and deposition studies. However, we devise that for more intricate analyses demanding higher precision, the integration of four-way couplings, and advanced numerical schemes, although with increased computational demands. We encourage users to carefully consider the scale and requirements of their specific research when choosing an appropriate model. Overall, our approach aims to strike a balance between practicality and precision, contributing to the accessibility of our model for a wide range of applications in fluid dynamics.

---

[1] S. A. Schumm and H. R. Khan, Experimental study of channel patterns, Geol. Soc. Am. Bull. **83**, 1755 (1972).

[2] S. Ikeda, G. Parker, and K. Sawai, Bend theory of river meanders. Part 1. Linear development, J. Fluid Mech. **112**, 363 (1981).

[3] A. Wesley Ward, Yardangs on mars: Evidence of recent wind erosion, J. Geophys. Res. **84**, 8147 (1979).

[4] A. W. Ward and R. Greeley, Evolution of the yardangs at Rogers Lake, California, Geol. Soc. Am. Bull. **95**, 829 (1984).

[5] P. Sanaei, Mathematical modeling of membrane filtration, Ph.D. thesis, New Jersey Institute of Technology, 2017, https://digitalcommons.njit.edu/dissertations/24/.

[6] P. Sanaei and L. J. Cummings, Membrane filtration with multiple fouling mechanisms, Phys. Rev. Fluids **4**, 124301 (2019).

[7] S. Y. Liu, Z. Chen, and P. Sanaei, Effects of particles diffusion on membrane filters performance, Fluids **5**, 121 (2020).

[8] Y. Sun, P. Sanaei, L. Kondic, and L. J. Cummings, Modeling and design optimization for pleated membrane filters, Phys. Rev. Fluids **5**, 044306 (2020).

[9] D. Persaud, M. Smirnov, D. Fong, and P. Sanaei, Modeling of the effects of pleat packing density and cartridge geometry on the performance of pleated membrane filters, Fluids **6**, 209 (2021).

[10] L. Ristroph, M. N. J. Moore, S. Childress, M. J. Shelley, and J. Zhang, Sculpting of an erodible body by flowing water, Proc. Natl. Acad. Sci. USA **109**, 19606 (2012).

[11] M. N. J. Moore, L. Ristroph, S. Childress, J. Zhang, and M. J. Shelley, Self-similar evolution of a body eroding in a fluid flow, Phys. Fluids **25**, 116602 (2013).

[12] M. N. J. Moore and J. Moore, Riemann-hilbert problems for the shapes formed by bodies dissolving, melting, and eroding in fluid flows, Commun. Pure Appl. Math. **70**, 1810 (2017).

[13] R. Jäger, M. Mendoza, and H. J. Herrmann, Channelization in porous media driven by erosion and deposition, Phys. Rev. E **95**, 013110 (2017).

[14] R. Jäger, M. Mendoza, and H. J. Herrmann, Mechanism behind erosive bursts in porous media, Phys. Rev. Lett. **119**, 124501 (2017).

[15] R. Jäger, M. Mendoza, and H. J. Herrmann, Clogging at pore scale and pressure-induced erosion, Phys. Rev. Fluids **3**, 074302 (2018).

[16] S. Bonelli, O. Brivois, R. Borghi, and N. Benahmed, On the modelling of piping erosion, Compt. Rend. Mécan. **334**, 555 (2006).

[17] S. Bonelli and N. Benahmed, Piping flow erosion in water retaining structures: inferring erosion rates from hole erosion tests and quantifying the failure time, *8th ICOLD European Club Symposium Dam Safety - Sustainability in a Changing Environment*, IECS 2010 (ATCOLD Austrian National Committee on Large Dams, 2010), p. 6.

[18] S. Bonelli, *Erosion in Geomechanics Applied to Dams and Levees* (John Wiley & Sons, New York, 2013).

[19] M. P. Dalwadi, I. M. Griffiths, and M. Bruna, Understanding how porosity gradients can make a better filter using homogenization theory, Proc. R. Soc. A: Math. Phys. Eng. Sci. **471**, 20150464 (2015).

[20] I. M. Griffiths, A. Kumar, and P. S. Stewart, Designing asymmetric multilayered membrane filters with improved performance, J. Membr. Sci. **511**, 108 (2016).

[21] I. M. K. Griffiths, A. Kumar, and P. S. Stewart, A combined network model for membrane fouling, J. Colloid Interface Sci. **432**, 10 (2014).

[22] P. Sanaei and L. J. Cummings, Flow and fouling in membrane filters: Effects of membrane morphology, J. Fluid Mech. **818**, 744 (2017).

[23] R. Fell, C. F. Wan, J. Cyganiewicz, and M. Foster, Time for development of internal erosion and piping in embankment dams, J. Geotechn. Geoen. Eng. **129**, 307 (2003).

[24] A. Wautier, S. Bonelli, and F. Nicot, Dem investigations of internal erosion: Grain transport in the light of micromechanics, Int. J. Numer. Anal. Methods Geomech. **43**, 339 (2019).

[25] A. López, M. T. Stickland, and W. M. Dempster, CFD study of fluid flow changes with erosion, Comput. Phys. Commun. **227**, 27 (2018).

[26] J. Zhao and T. Shan, Numerical modeling of fluid-particle interaction in granular media, Theor. Appl. Mech. Lett. **3**, 021007 (2013).

[27] K. Weishaupt, A. Terzis, I. Zarikos, G. Yang, M. de Winter, and R. Helmig, Model reduction for coupled free flow over porous media: A hybrid dimensional pore network model approach, arXiv:1908.01771.

[28] A. Q. Raeini, B. Bijeljic, and M. J. Blunt, Generalized network modeling of capillary-dominated two-phase flow, Phys. Rev. E **97**, 023308 (2018).

[29] Z. Yu and L.-S. Fan, Lattice Boltzmann method for simulating particle–fluid interactions, Particuology **8**, 539 (2010).

[30] C. Zahasky, S. J. Jackson, Q. Lin, and S. Krevor, Pore network model predictions of darcy-scale multiphase flow heterogeneity validated by experiments, Water Resour. Res. **56**, e2019WR026708 (2020).

[31] S. Bonelli and O. Brivois, The scaling law in the hole erosion test with a constant pressure drop, Num. Anal. Meth. Geomech. **32**, 1573 (2008).

[32] M. J. Chen, L. S. Kimpton, J. P. Whiteley, M. Castilho, J. Malda, C. P. Please, S. L. Waters, and H. M. Byrne, Multiscale modelling and homogenisation of fibre-reinforced hydrogels for tissue engineering, Eur. J. Appl. Math. **31**, 143 (2020).

[33] M. Malvè, D. J. Bergstrom, and X. B. Chen, Modeling the flow and mass transport in a mechanically stimulated parametric porous scaffold under fluid-structure interaction approach, Int. Commun. Heat. Mass Trans. **96**, 53 (2018).

[34] P. Kumar and G. P. Raja Sekhar, Mathematical modeling of elastodynamics and cell growth inside a deformable scaffold fitted to the periphery of a bioreactor, Math. Meth. Appl. Sci. **44**, 7304 (2021).

[35] I. Fatt, The network model of porous media, Trans. AIME **207**, 144 (1956).

[36] S. D. Rege and H. Scott Fogler, Network model for straining dominated particle entrapment in porous media, Chem. Eng. Sci. **42**, 1553 (1987).

[37] M. A. Ioannidis and I. Chatzis, Network modelling of pore structure and transport properties of porous media, Chem. Eng. Sci. **48**, 951 (1993).

[38] P. Sanaei and L. J. Cummings, Membrane filtration with complex branching pore morphology, Phys. Rev. Fluids **3**, 094305 (2018).

[39] B. Gu, D. L. Renaud, P. Sanaei, L. Kondic, and L. J. Cummings, On the influence of pore connectivity on performance of membrane filters, J. Fluid Mech. **902**, A5 (2020).

[40] Z. Chen, S. Y. Liu, I. C. Christov, and P. Sanaei, Flow and fouling in elastic membrane filters with hierarchical branching pore morphology, Phys. Fluids **33**, 062009 (2021).

[41] P. Sanaei, L. J. Cummings, S. L. Waters, and I. M. Griffiths, Curvature-and-fluid-stress-driven tissue growth in a tissue-engineering scaffold pore, Biomech. Mod. Mech. **18**, 589 (2019).

[42] D. Lachouette, F. Golay, and S. Bonelli, One-dimensional modeling of piping flow erosion, Compt. Rend. Mécanique **336**, 731 (2008).

[43] F. Golay and S. Bonelli, Numerical modeling of suffusion as an interfacial erosion process, Eur. J. Env. Civil Eng. **15**, 1225 (2011).

[44] S.-H. Chiu, M. N. J. Moore, and B. Quaife, Viscous transport in eroding porous media, J. Fluid Mech. **893**, A3 (2020).

[45] G. I. Taylor, Dispersion of soluble matter in solvent flowing slowly through a tube, Proc. R. Soc. London A **219**, 186 (1953).

[46] B. D. Quaife and M. N. J. Moore, A boundary-integral framework to simulate viscous erosion of a porous medium, J. Comput. Phys. **375**, 1 (2018).

[47] P. Sanaei, G. W. Richardson, T. Witelski, and L. J. Cummings, Flow and fouling in a pleated membrane filter, J. Fluid Mech. **795**, 36 (2016).

[48] D. Fong, L. J. Cummings, S. J. Chapman, and P. Sanaei, On the performance of multilayered membrane filters, J. Eng. Math. **127**, 23 (2021).